Geophysical Prospecting, 2000, **48**, 63–85

GPR study of pore water content and salinity in sand[1]

S.A. al Hagrey[2,3] and C. Müller[2,4]

Abstract

High-resolution studies of hydrological problems of the near-surface zone can be better accomplished by applying ground-probing radar (GPR) and geoelectrical techniques. We report on GPR measurements (500 and 900 MHz antennae) which were carried out on a sorted, clean sand, both in the laboratory and at outdoor experimental sites. The outdoor sites include a full-scale model measuring $5 \times 3 \times 2.4\,m^3$ and a salinity site measuring $7.0 \times 1.0 \times 0.9\,m^3$ with three buried sand bodies saturated with water of various salinities. Our studies investigate the capability of GPR to determine the pore water content and to estimate the salinity. These parameters are important for quantifying and evaluating the water quality of vadose zones and aquifers. The radar technique is increasingly applied in quantifying soil moisture but is still rarely used in studying the problems of water salinity and quality.

The reflection coefficient at interfaces is obtained from the amplitude spectrum in the frequency and time domains and is confirmed by 1D wavelet modelling. In addition, the GPR velocity to a target at a known depth is determined using techniques of two-way traveltime, CMP semblance analysis and fitting an asymptotic diffraction curve.

The results demonstrate that the reflection coefficient increases with increasing salinity of the moisture. These results may open up a new approach for applications in environmental problems and groundwater prospecting, e.g. mapping and monitoring of contamination and evaluating of aquifer salinity, especially in coastal areas with a time-varying fresh-water lens. In addition, the relationship between GPR velocity and water content is established for the sand. Using this relationship, a subsurface velocity distribution for a full-scale model of this sand is deduced and applied for migrated radargrams. Well-focused diffractions separate single small targets (diameter of 2–3 cm, at a depth of 20–180 cm and a vertical interval of 20 cm). The results underscore the high potential of GPR for determining moisture content and its variation, flow processes and water quality, and even very small bodies inside the sand or soil.

---

[1] Received March 1998, revision accepted July 1999.

[2] Institute of Geosciences, Department of Geophysics, Christian-Albrechts-Universität, Olshausenstrasse 40–60, 24118 Kiel, Germany.

[3] E-mail: sattia@geophysik.uni-kiel.de

[4] E-mail: cmueller@geophysik.uni-kiel.de

Introduction

The demand for high-resolution studies of hydrological problems in both unsaturated vadose soil zones and the underlying aquifer layers is increasing rapidly. Applications are currently found in both conventional groundwater prospecting and in new environmental and geotechnical fields. These include mapping, monitoring and quality evaluation of pore water salinity and contamination as well as studying flow processes in the unsaturated and saturated zones. In coastal and island environments, the fresh-water aquifer is typically of small extent with irregular form and occurs as a thin lens floating on dense saline water, known as the Ghyben–Herzberg fresh-water lens (Ghyben 1888; Herzberg 1901; Bugg and Lloyd 1976; Cant and Weech 1986) (Fig. 1). A transition zone, with salinity increasing gradually with depth, separates the fresh-water lens from the underlying saline zone. Evaluating water resources in such settings is difficult because of time-varying hydrological conditions (e.g. through water exploitation) and aquifer heterogeneity. Electrical resistivity techniques are traditionally used for evaluating groundwater potentials (e.g. Fretwell and Stewart 1981), but results are often uncertain. Besides the well-known ambiguity of data interpretation, resistivity techniques have a limited resolving power in mapping subsurface aquifers of small and variable size. Also, the possible trade-off between several parameters (water and matrix resistivity, porosity) in Archie's equation (Archie 1942) renders the evaluation of reservoir salinity difficult (Worthington 1976). In a granular aquifer (free of clay) Archie's equation (Archie 1942) states that

$$\rho_w = a^{-1}\rho_b\phi^m, \tag{1}$$

where ρ_b, ρ_w denote bulk and pore water resistivities, respectively, ϕ denotes porosity in volume fraction, a is a constant depending on the pore geometry ($a = 1$ for saturation $S \geq 0.25$ (Schön 1983)), and m is a cementation factor, depending on particle shape ($m = 1.5–2$ for spherical-to-oblate sediments (Wyllie and Gregory 1953; Jackson, Taylor Smith and Stanford 1978)).

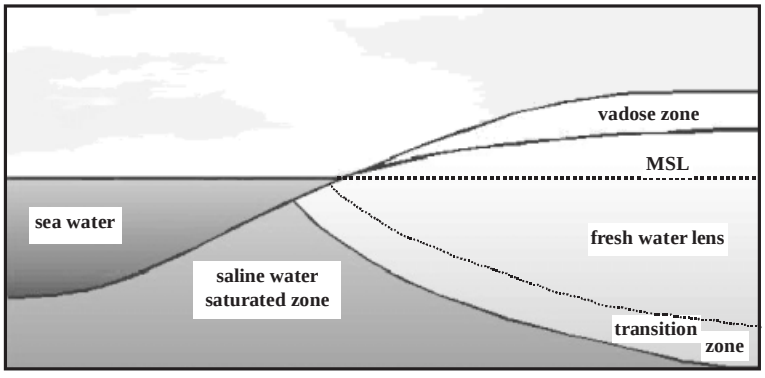

Figure 1. A fresh-water lens (Ghyben–Herzberg lens) in the coastal zone. MSL, mean sea level.

Table 1. A saturated formation interpreted as either a fresh or brackish aquifer depending on the porosity value which lies within the normal error bar. ρ_b, ρ_w are the bulk and pore water resistivity, respectively, ϕ is the porosity in volume fraction.

Aquifer water	ρ_b (Ωm)	ϕ	ρ_w (Ωm) from (1)	Salinity* (ppm)
Fresh water**	54.00	0.25	≥ 3.40	≤ 1500
Brackish water	54.00	0.20	2.10	2120

* from salinity–ρ_w relationship (e.g. Keller and Frischknecht 1966); **standards of World Health Organization (Bouwer 1978).

The aquifer-water salinity is deduced from ρ_w (e.g. Keller and Frischknecht 1966), which can be determined from (1) if ρ_b and ϕ are known from electrical and hydrological measurements. For example, in calcareous aquifers ($a = 1$, $m = 2$), the same saturated zone with $\rho_b = 54\,\Omega$m can be interpreted either as a fresh-water aquifer (salinity (NaCl equivalent) ≤ 1500 ppm; $\rho_w \geq 3.40\,\Omega$m) for $\phi = 0.25$, or as brackish water (salinity ≤ 2120 ppm; $\rho_w = 2.20\,\Omega$m) for $\phi = 0.2$ (Table 1). The small difference is insufficient to distinguish between fresh and brackish water in view of the normal error range of $\sim 20\%$ in the techniques applied and thus makes the interpretation ambiguous.

High-resolution techniques are applied in studying environmental problems such as transport and storage of a contaminant in the vadose zone and the underlying aquifer layer. For example, the extensive use of agrochemicals (including toxic substances such as pesticides) poses a serious danger for the environment if these are not fully degraded by plants. A detailed study of the flow nature, including flow type (uniform or preferential), paths and velocity, highlights the need for better understanding of the hydrological aspects of the soil material (Hagrey and Michaelsen 1996, 1999). For studying as many aspects as possible, a set of infiltration experiments were carried out using tap water spiked with a non-reactive tracer of differing concentrations in a full-scale model and *in situ* (Hagrey *et al.* 1998, 1999). In addition to the percolation methods (e.g. tensiometer and time-domain reflectometry (TDR) for determining water potential and water content, respectively), high-resolution techniques of ground-probing radar (GPR) and DC resistivity are applied in the experiments. The main goal is to monitor the water content, water flow and solute movement in the subsurface.

This paper deals with part of the high-resolution GPR studies of 500 and 900 MHz antennae in the laboratory and at two outdoor experimental sites. The study is carried out on a clean, sorted sand as a function of pore water saturation and at various salinities. The propagation of electromagnetic (EM) waves depends mainly on the dielectric constant ϵ and the DC conductivity σ of the medium. These parameters are controlled by the pore water saturation S and the salinity (or water resistivity ρ_w) and angular frequency ω. The radar technique is increasingly applied in mapping the water content in the near-surface zone but is still rarely used in studying the water salinity (e.g. Olhoeft 1987; Wensink 1993). Therefore, this study aims at investigating the

applicability of radar for detecting and quantifying the water content and salinity through their effects on the propagation parameters such as velocity (traveltime), reflection coefficient, etc. We have also attempted to improve the understanding and solution of the above-mentioned trade-off between hydrological parameters of water and matrix resistivity and porosity. An exact evaluation of salinity may open up a new application of high-resolution studies for detecting and monitoring of saline-water intrusion and general groundwater pollution. This paper reports on the progress made in solving the problem under study, on the lessons learned and on the recommendations which will lead to improved results in further investigations.

EM wave propagation parameters and electrical properties

We now give a brief review of the theory required for the interpretation of GPR data in terms of soil parameters. The propagation of GPR signals in a homogeneous and isotropic medium can be described by the plane-wave solution of the Helmholtz equation which is obtained from Maxwell's equations (Ward and Hohmann 1988; Hayt 1989). The solution for one component of the electric field intensity vector **E** travelling in the z-direction is

$$E = E_0\, \mathrm{e}^{-\alpha z}\, \mathrm{e}^{\mathrm{j}(\omega t - \beta z)}, \tag{2}$$

where α is an attenuation constant, β is a phase constant, $\omega = 2\pi f$ is angular frequency (in s^{-1}) and f is frequency (in s^{-1}).

The velocity and attenuation are the main parameters describing the GPR wave propagation. Both depend on the dielectric and conductivity properties of the material. In general the complex dielectric permittivity ϵ (or dielectric constant) is given by (Sen, Scala and Cohen 1981; Davis and Annan 1989)

$$\epsilon = \epsilon' - \mathrm{j}\epsilon'', \tag{3}$$

where ϵ', ϵ'' are the real and imaginary parts of the complex dielectric permittivity, respectively (in F/m).

It is useful to separate ϵ'' into the high-frequency component ϵ''' associated with the relaxation response phenomena, and the DC conductivity component σ/ω (σ denotes conductivity (in S/m)), so that

$$\epsilon'' = \epsilon''' + \frac{\sigma}{\omega}. \tag{4}$$

We deal with conductivities ranging from 10 to 1000 mS/m and frequencies ranging from 10 to 1000 MHz. Therefore, we may skip the high-frequency component associated with the relaxation response phenomena (ϵ''') and keep the DC conductivity component of the imaginary or loss part of the dielectric permittivity. Then we obtain, from (3) and (4),

$$\epsilon = \epsilon_0 \epsilon_\mathrm{r} = \epsilon_0(\epsilon_\mathrm{r}' - \mathrm{j}\epsilon_\mathrm{r}'') = \epsilon_0 \left(\epsilon_\mathrm{r}' - \mathrm{j}\frac{\sigma}{\omega\epsilon_0}\right), \tag{5}$$

where ϵ_r denotes the relative dielectric permittivity, ϵ_0 denotes the permittivity of free space ($=8.854 \cdot 10^{-12}$ F/m), $\epsilon_r' = \epsilon'/\epsilon_0$ and $\epsilon_r'' = \epsilon''/\epsilon_0$ denote the real and imaginary (or loss) parts of ϵ_r, respectively.

In this case the dielectric loss can be expressed as

$$\tan\theta = \frac{\epsilon''}{\epsilon'} = \frac{\sigma}{\omega\epsilon_0\epsilon_r'}, \tag{6}$$

where θ denotes the loss angle.

For $\tan\theta << 1$, the dielectric loss can be neglected, since the diffusion term and dispersive effects through $\epsilon(\omega)$ in a wet medium are negligible. In our case $\tan\theta \approx 1$ and therefore will be retained in the calculations.

The attenuation and phase constants from (2) can now be combined into the complex propagation constant k, given by

$$k = \beta - j\alpha = \sqrt{\omega^2\epsilon'\mu - j\omega\mu\sigma}, \tag{7}$$

where μ denotes magnetic permeability (in H/m).

In order to obtain the skin depth δ and the phase velocity v, the attenuation and phase constants can be expressed separately. Both are real quantities, given by

$$\alpha = \frac{1}{\delta} = \omega\sqrt{\frac{\mu\epsilon'}{2}\left(\sqrt{1+\tan^2\theta}+1\right)} \tag{8}$$

and

$$\beta = \omega\sqrt{\frac{\mu\epsilon'}{2}\left(\sqrt{1+\tan^2\theta}-1\right)}. \tag{9}$$

The phase velocity of a wave propagating in the z-direction in the case of $\tan\theta \approx 1$ is given by

$$v = \frac{\omega}{\beta}. \tag{10}$$

At low conductivities (< 100 mS/m, $\tan\theta << 1$) and frequencies of 10–1000 MHz, the velocity remains essentially constant so that the radar signal velocity in low-loss materials is given by

$$v \approx \frac{c}{\sqrt{\epsilon_r'}}. \tag{11}$$

At a plane interface separating two homogeneous and isotropic half-spaces, the reflection coefficient R for normal incidence is defined as

$$R = \frac{Z_2 - Z_1}{Z_2 + Z_1}, \tag{12}$$

where Z is the intrinsic impedance which becomes a complex quantity when the DC conductivity σ cannot be neglected, so that

$$Z = \frac{\omega\mu}{k} = \sqrt{\frac{j\omega\mu}{\sigma + j\omega\epsilon'}}. \tag{13}$$

Obviously the propagation of GPR signals is dominated by the relative permittivity and the DC conductivity of the medium. Since the effect of saturation on the relative permittivity is dominant, the reflection amplitude of the GPR signal gives an estimate of the water content of the underlying layer. The DC conductivity which is directly proportional to the salinity strongly affects the skin depth of the radar signal (Wensink 1993) and the reflection coefficient. An upper aquifer boundary with Z_2 (aquifer) $< Z_1$ (overburden) has a negative reflection coefficient ($R<0$). This contrast is a potential target for GPR which will be studied in the next section.

Soil properties from radar (GPR)

CRIM equation

A formulation commonly used for analysing petrophysical parameters is the complex refraction index method (CRIM) which is the electrical analogue of the Wyllie time-average equation (e.g. Guéguen and Palciausskas 1994). The EM propagation slowness (inverse of velocity and directly proportional to the square root of the relative dielectric constant, see (11)) through a composite material of partially saturated soils (with solid grains, water and air) is expressed by

$$\sqrt{\epsilon_{\mathrm{r,b}}} = \phi S\sqrt{\epsilon_{\mathrm{r,w}}} + (1-\phi)\sqrt{\epsilon_{\mathrm{r,g}}} + \phi(1-S), \tag{14}$$

where $\epsilon_{\mathrm{r,b}}, \epsilon_{\mathrm{r,g}}, \epsilon_{\mathrm{r,w}}$ denote the relative dielectric constants of the bulk sample, grain and water, respectively.

The CRIM of the mixture theory asserts that the CRI of the mixture $\sqrt{\epsilon_{\mathrm{r,b}}}$ is the volumetric sum of the CR indices of all components. Full saturation ($S=1$) results in a simplified form of (14) for a two-component mixture of water and grain.

Hanai–Bruggeman formula

This equation relates ϵ_{r}, and ϕ of partially and fully saturated soils (Sen 1981; Endres and Knight 1992). This method, which is based on the effective medium theory, can also be used to predict the effective dielectric response of partially saturated soil samples (Endres and Knight 1992). The effective dielectric response of a partially saturated medium (grains, fluid and air) is obtained from the complex dielectric response of the pore fillers (water/air mixture) and of the bulk material (by adding mineral grains to the mixture), i.e.

$$\epsilon_{\mathrm{r,p}} = \epsilon_{\mathrm{r,w}} S^{m1}\left(\frac{\epsilon_{\mathrm{r,p}}(\epsilon_{\mathrm{r,w}}-1)}{\epsilon_{\mathrm{r,w}}(\epsilon_{\mathrm{r,p}}-1)}\right)^{m1}, \tag{15}$$

$$\epsilon_{\mathrm{r,b}} = \epsilon_{\mathrm{r,p}} \phi^{m2}\left(\frac{\epsilon_{\mathrm{r,b}}(\epsilon_{\mathrm{r,p}}-\epsilon_{\mathrm{r,g}})}{\epsilon_{\mathrm{r,p}}(\epsilon_{\mathrm{r,b}}-\epsilon_{\mathrm{r,g}})}\right)^{m2}, \tag{16}$$

where $\epsilon_{\mathrm{r,p}}$ denotes the relative dielectric constant of pores, $m1$, $m2$ denote the cementation exponents which are related to the shape of the air bubble and mineral grains, respectively, and $m1$ is a function of saturation.

For a saturated sample (two phases of grain/water mixture), the calculation of the bulk dielectric response is reduced to a single equation (16) where $\epsilon_{r,w} = \epsilon_{r,p}$.

Topp equation

It is impossible in practice to derive both porosity ϕ and saturation S from the dielectric constant. Topp, Davis and Annan (1980) used a wide range of soil samples with varying degrees of water saturation to derive the following relationship between the relative dielectric constant $\epsilon_{r,b}$ and the water content G:

$$\epsilon_{r,b} = 3.03 + 9.3G + 146.0G^2 - 76.7G^3. \quad (17)$$

Experimental sand

Washed and roughly sieved quarry sand is used in this study. Several samples of this sand were analysed in the laboratory to determine their physical and hydrological parameters (Table 2). A combined sieve and pipette technique yields a sorted, homogeneous grain-size distribution (fine to medium, bimodal, 97.38%) thus a nearly clean sand (silt and clay components = 1.18% only) (Schachtschabel *et al.* 1992). The sand has bulk and grain densities of 1.472 g/cm^3 and 2.762 g/cm^3, respectively. The effective porosity ϕ (of water-filled pores) lies in the range 0.32–0.37. This range may be related to the degree of compactness of the sand grains and the measurement error in the individual samples. The water content is measured using the TDR technique and sampling with a metallic cylinder.

Experimental sites

The experiments were carried out on the sand described above (Table 2) in the laboratory and at two outdoor sites: the full-scale model and the experimental salinity site.

The full-scale model

This site (x, y, z dimensions of $5 \times 3 \times 2.4$ m^3) is used for controlled infiltration experiments simulating flow processes within the unsaturated vadose zone (Figs 2a and b,

Table 2. Measured parameters of the sand (Hagrey *et al.* 1998).

Parameter	Quantity
Fraction of fine grain size (63–200 μm)	31.714%
Fraction of medium grain size (200–630 μm)	65.661%
Grain density (g/cm^3)	2.762
Bulk density (g/cm^3)	1.472
Hydraulic conductivity k_f (cm/s)	1.275×10^{-2}
Effective porosity ϕ (fraction volume)	0.32–0.37

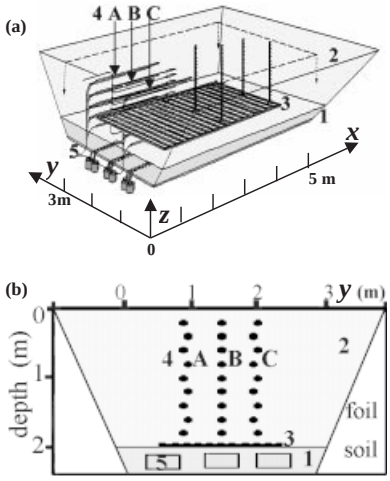

Figure 2. Overview of experimental set-up of full-scale model: (a) block diagram and (b) vertical section. 1: Filtered gravel horizon; 2: a homogeneous sand of Table 2; 3: electrode grid; 4: A, B, C profiles of tensiometers and TDR sensors; 5: bottom drain.

Hagrey *et al.* 1998). The model base consists of a 0.4 m-thick filter layer of gravel. Overlying this filter, the model is filled (up to 2 m thickness) with the sand described in Table 2. The model is installed with several hydrological and geophysical sensors distributed at various depths, e.g. a horizontal electrode grid at a depth of 2 m and 27 sensors of the tensiometer and TDR (three vertical profiles with nine instruments each at a depth interval of 0.2 m, see following sections).

The experimental salinity site

At this site (x, y, z dimensions of $7.0 \times 1.0 \times 0.9\,m^3$), four plastic bodies (one air and three water-saturated sand containers) and one metallic plate were buried in the sand described in Table 2 (Figs 3a and b). The pore saturant of the three sand containers is fresh, brackish and saline water with a decrease in the corresponding water and bulk resistivities in the same configuration order (Table 3).

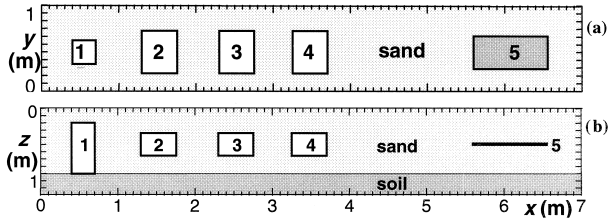

Figure 3. The experimental salinity site with buried bodies. (a) Horizontal section; (b) vertical section (see Table 3 for symbols).

Table 3. Bodies buried in the experimental salinity site of the radar measurements.

Body number	1	2	3	4	5
Description	Air container	Sand saturated with			Metallic plate
		Saline water	Brackish water	Fresh water	
Dimension (cm)	$30\times30\times60$	$45\times54\times31$	$45\times54\times31$	$45\times54\times31$	$95\times42\times0.2$
Depth (cm)	30.00	35.00	35.00	35.00	50.00
DC water resistivity ρ_w (Ωm)	–	0.20	1.10	13.50	–
DC bulk resistivity ρ_b (Ωm)	$\propto$	1.74	6.99	66.67	1×10^{-7}

Pore water salinity from radar

Radar measurements at the experimental salinity site

On the site surface, using a 500 MHz antenna, radargrams were measured along profiles parallel to the x-axis and at spacing of 0.2 m along the y-axis (one example is shown in Fig. 4). The study is concentrated mainly on the water-saturated bodies, using the metallic plate with a reflection coefficient of $R = -1$ as reference.

A qualitative interpretation of the radargrams yields the following primary results:

- Reflections from the top of all water-saturated sand bodies (R2–4, at $t = 7$ ns) and the metallic plate (R5, $t = 9.5$ ns) show a negative reflection coefficient R. The negative R is caused by the lower impedance of the single bodies relative to that of the overburden sand (i.e. $Z_2 < Z_1$ as is found from (12) and (13)). By contrast, reflections from the top of the air container show a positive R due to its positive impedance contrast with respect to the surrounding sand.
- The reflection amplitude R increases with the salinity of the pore water, i.e. with σ_w. For the water-saturated sand bodies, R is a maximum for saline water, intermediate for brackish water and a minimum for fresh water.
- Only the lower boundary of the fresh-water body shows obvious reflections (B4, at $t = 15.5$ ns). The lower boundaries of the brackish- and salt-water bodies display no clear reflections. The reason may be related to the higher energy absorption of GPR waves in such a conductive medium, i.e. the limited skin depth. The lower boundary of the air container cannot be uniquely resolved from the upper one due to the high GPR velocity in air (30 cm/ns).
- The strong reflections of radar signals from the metallic plate (R5, $t = 9.5$ ns, depth $z = 50$ cm) show well-defined multiples (M5 and M5′ at $t = 19$ ns and 28 ns, respectively). The two-way traveltime yields an average radar velocity v of 15 cm/ns for the overburden sand.

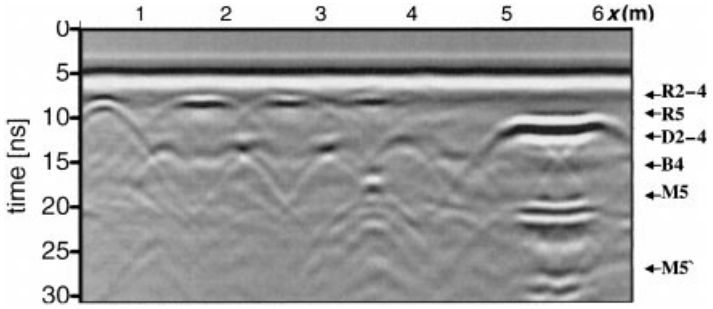

Figure 4. A radargram profile parallel to the x-axis (at $y = 0.5$ m) registered with a 500 MHz antenna. R2–4, D2–4 indicate the reflections from the top and diffractions from outer lower edges of bodies 2–4, respectively. B4 indicates reflections from the bottom of body 4. R5, M5, M5′ indicate reflections and first and second multiples from body 5, respectively.

- The diffractions from the outer lower edges of the water-saturated bodies (D2–4, $z = 65$ cm) are seen at $t = 13$ ns in the gaps separating one body from another along the x-axis.

Analysis of reflected wavelets from the radargram

Reflections from the interface separating the overburden sand from the different individual bodies are investigated in detail on single traces of the radargram. Traces are band-pass filtered (100–900 MHz). The wavelets reflected at the top of the bodies can be identified well on the radargram. Five single traces from the reflection train of each body are plotted in the time domain (Fig. 5a). All individual reflected wavelets show a consistent waveform. The amplitudes are similar within the same body and differ from one body to another. A weak amplitude dependence on salinity can be seen.

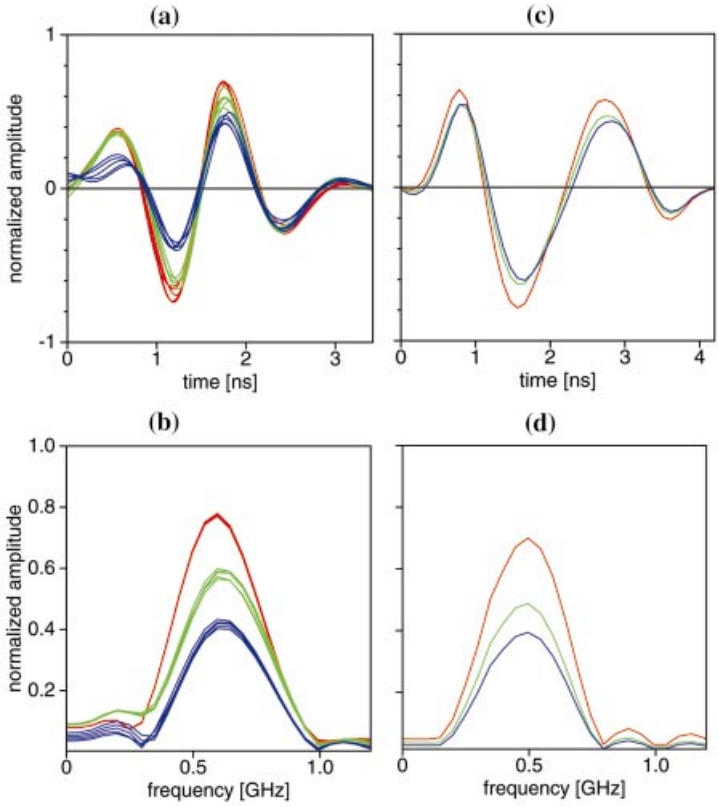

Figure 5. Wavelets reflected from the individual water-saturated bodies of Fig. 2. The amplitude is normalized relative to that of the metallic plate with a reference reflection coefficient of −1. Red denotes a saline-water body, green denotes a brackish-water body, blue denotes a fresh-water body. (a) (b) Measured wavelets in the time and frequency domains, respectively. (c) (d) Calculated wavelets in the time and frequency domains, respectively.

The saline-water body shows the maximum amplitude, the brackish-water body an intermediate amplitude and the fresh-water body the minimum amplitude. However, this amplitude difference is less than 20% of the highest amplitude of salt water and may thus lie within the range of field noise.

Differences in the reflection amplitudes from the three water-saturated bodies are studied by analysing the reflected wavelets in the frequency domain. The amplitude spectra of the three water-saturated sand bodies (Fig. 5b) show identical bandwidth (400 MHz) and centre frequency (550 MHz) at maximum amplitude. Note the stronger dependence of the amplitude on the pore water salinity in the frequency domain than in the time domain. Thus, the three bodies can be more easily distinguished from one another on the basis of the reflection amplitude in the frequency domain than in the time domain (see Figs 5a and b).

Analysis of basic reflected wavelets from modelling

A basic wavelet reflected at the top of the different bodies is calculated using 1D forward modelling for a two-layer case (Göttsche 1997). This two-layer assumption (a dry sand overburden underlain by the body) is justified by the high resolution power of the radar technique. The input parameters needed are the complex dielectric constant ϵ, the DC conductivity σ and the upper layer thickness (Tables 3 and 4). The real part of the relative complex dielectric constant ϵ_r' for dry and saturated sand is obtained from the CRIM equation (14) for full saturation by replacing the measured porosity ϕ value from Table 2. The input wavelet has a centre frequency of 450 MHz and a bandwidth of 300 MHz. The resulting wavelets reflected at the top of the individual bodies (in the time and frequency domains) have the same polarity and negative reflection coefficient as the input wavelet (Figs 5c and d). Again the amplitude increases with the salinity of the body. It is obvious that the relative wavelet amplitude from a single body can be better separated in the frequency domain than in the time domain (compare Figs 5a and b and Figs 5c and d). We conclude that the discrimination between aquifers of different water salinity is more readily achieved in the frequency domain than in the time domain.

The energy in both the time and frequency domains has to be identical according to the Parseval theorem (Buttkus 1991). For discrete functions this theorem takes

Table 4. Parameters of wavelet modelling for the dry sand and buried bodies described in Table 3. σ: DC conductivity; ϵ_r', ϵ_r'': real and imaginary relative dielectric constants, respectively.

	Dry sand	Body 2	Body 3	Body 4	Body 5
σ (mS/m)	0.28	575	143	15	1×10^{10}*
ϵ_r'	2.40	26.52	26.52	26.52	5
ϵ_r''	0.01	20.67	5.14	0.54	1×10^{7}

* Lorrain *et al.* (1995).

the form

$$\sum_{j=0}^{N-1} |x_j|^2 = \frac{1}{N} \sum_{k=0}^{N-1} |\hat{x}_k|^2, \tag{18}$$

where $\Sigma_{j=0}^{N-1} |x_j|^2$ and $(1/N)\,\Sigma_{k=0}^{N-1} |\hat{x}_k|^2$ are the energies of the time and frequency domains, respectively.

The graphs of the time and frequency domains display the parameters x_j and $\hat{x}_k$, respectively (Fig. 5). Consequently, the energy correlation between the time and frequency domains should take into consideration, in addition to the terms $\Sigma_{j=0}^{N-1} |x_j|^2$ and $\Sigma_{k=0}^{N-1} |\hat{x}_k|^2$, the constant $1/N$ in the frequency domain.

Reflection coefficient R

The reflection coefficient of the individual bodies is obtained from the amplitude spectra of wavelets (i.e. in the frequency domain) which are normalized with respect to the reflected wavelet amplitude of the metallic plate ($R = -1$). The results for the measured and calculated wavelets are plotted together with the relative differences (Fig. 6). It is clear that the fitted reflection curve increases with salinity of the pore water. A satisfactory agreement is obtained between the observed and calculated reflection coefficients. The maximum relative difference is only 0.2. An improved resolution may be achieved by determining the degree of saturation in the overburden and aquifer and by taking into account the dependence of ϵ_r on the frequency and DC conductivity (Wensink 1993; Lorrain, Corson and Lorrain 1995). In the present study, the water-saturated sand bodies vary only in ϵ_r'' (imaginary part of ϵ_r). This is further

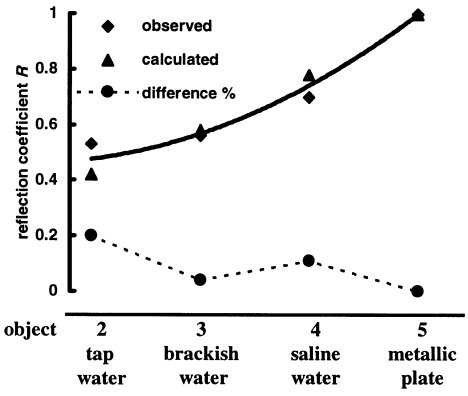

Figure 6. Normalized reflection coefficients R and relative differences between measured and calculated wavelets (fitted continuous and dashed lines, respectively). Wavelets are reflected at the interface between the overburden sand and water-saturated bodies. R is normalized to that of the metallic plate.

investigated for the case where differences in ϵ_r' (real part of ϵ_r) yield a large contrast in R.

We can conclude in general that the radar technique can be used for distinguishing near-surface zones with pore water of different salinity concentrations. However, for applications in evaluating aquifer water and mapping of contamination, the technique still requires further development, especially for resolving the effects of field and geological noise under conditions of a low signal/noise ratio. Further efforts should cover a finer increment in salinity and allow for the possibility of predicting an empirical relationship between R and salinity for different types of earth material.

GPR velocity

GPR velocity for the sand of the experimental salinity sites

Radargrams measured at the experimental salinity site show well-developed diffraction hyperbolae originating from the different bodies of known depth of burial (Table 3, Fig. 3). The velocity analysis is carried out by fitting an asymptotic curve to these hyperbolae (Stolte 1994). The analysis yields a velocity of 16 cm/ns for the near-surface sand (from the surface down to the top of bodies) and 6 cm/ns for fresh-water-saturated sand body (Table 5). The latter velocity is calculated as 6.0 cm/ns ($\epsilon = 25$) by the two-layer migration analysis of a finite reflection window for the fresh-water body 4 (Göttsche 1997). This value is in good agreement with the range of $20 \leq \epsilon \leq 30$ for water-saturated sand.

GPR velocity for the sand of the full-scale model

On the surface of the full-scale experimental site, 16 CMP gathers were measured using 500 MHz antennae. The gathers were carried out along the middle x-axis profile ($y = 1.5$ m), where they began with an offset of 60 cm and increased at intervals of 10 cm. A CMP semblance velocity analysis for the strong events of the lower electrode grid (at 2 m depth) yields an rms velocity v_{rms} of 15 cm/ns (typical for near-surface sand (e.g. Davis and Annan 1989)). This v_{rms} value agrees with that obtained from laboratory data for the same sand with 10% saturation (see next sections). This saturation value is confirmed from TDR measurements of water content in the full-scale model (Hagrey *et al.* 1998). The CMP velocity model (Fig. 7) shows horizontal thin layers of velocities varying only with depth (velocity = 13–16 cm/ns ± 1–2.5 cm/ns, semblance = 0.95). To compare CMP velocity with TDR and tensiometer data (of

Table 5. The GPR velocity from diffraction hyperbolae of the bodies described in Table 3 (see Fig. 3 for symbols).

Body no.	5	Top of 2–4	Bottom of 4	Top of 1
Diffraction symbol	(R5, M5, M5′)	(R2–4)	(B4)	
v (cm/ns) ± 1 cm/ns	16	16	6	16

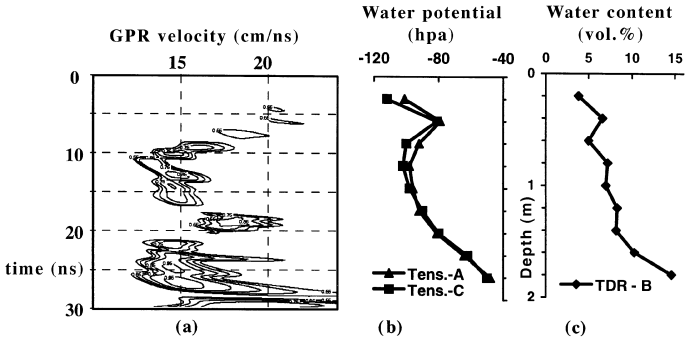

Figure 7. Results of *in situ* measurements in the sand of the experimental site of the full-scale model. (a) The GPR velocity from the spectrum of CMP points (isoline of semblance), 500 MHz antenna. (b) The water potential from tensiometer measurements. (c) The water content from TDR measurements. Note that the velocity distribution with depth generally has an inverse and a direct proportionality to the water potential and water content, respectively.

water content and water potential, respectively), the time axis of the radargrams is roughly adjusted at the depth axis of the TDR and tensiometer curves; reflection events from the lower grid at $t = 27$ ns correspond to a depth of 2 m. In general the radar velocity is inversely proportional to water content and water potential. This well-known inverse proportionality between moisture content and GPR velocity (e.g. Greaves *et al.* 1996) is investigated on an identical sand sample in the laboratory in the next section.

GPR velocity versus water content in the laboratory

In the laboratory experiment the bulk velocity v_b of GPR waves was measured as a function of pore water content G. A plastic container ($35 \times 26 \times 31$ cm^3) was filled with dry sand (initial water content $G = 0$ in volume fraction) taken from the experimental site (Table 2). For the sand sample, the total pore volume (corresponding to full saturation of $G = 0.33$) was calculated from the predetermined sample weight and volume using the sand porosity and density values from Table 2. Beginning with the dry sand, saturation-dependent measurements were carried out with G increasing in the range 0–0.33 at increments of about 0.02. New saturation stages were initiated by adding the predetermined water volume (corresponding to the G-increment) to the mixture of the preceding stage and by mixing both liquid and solid phases strongly until good homogenization was achieved. For each saturation step, traces of radar signals reflected from the underlying metallic plate were recorded using 500 and 900 MHz antennae.

Figure 8 shows examples of the data for 500 MHz ($G = 0.14$) and 900 MHz ($G = 0.28$). The radargrams exhibit well-separated events of the direct air wave ($t = 0$ ns) followed by the reflections and multiples at the corresponding times ($t = 6$ ns, 12 ns) for the 900 MHz antenna and ($t = 6.5$ ns, 15.5 ns) for the 500 MHz antenna. Only

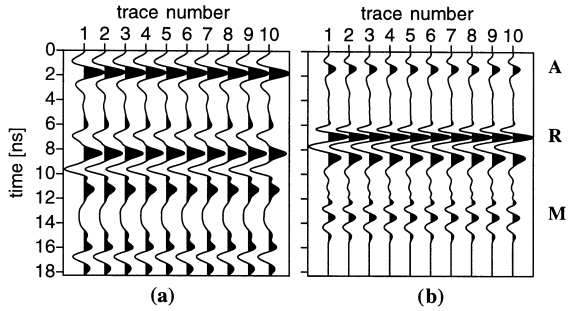

Figure 8. (a) 500 MHz radar traces at water content $G = 28$ vol.%; (b) 900 MHz radar traces at water content $G = 14$ vol.%. A, R, M denote reflections from the air–sand interface, metallic plate and multiple, respectively. Note that M of the 500 MHz radargram interfere with and are masked by low-frequency signals.

multiples of the 500 MHz radargram interfere with and are masked by low-frequency signals. Both air and reflected waves show a negative polarity resulting from interfaces with a negative reflection coefficient. The positive polarity of multiples originates from the double reflections from the metallic plate with $R = -1$. Compared with the 900 MHz data, the 500 MHz radargram shows similar results with later arrival times for the reflected wave ($t = 6.5$ ns) and the multiple ($t = 15.5$ ns). The 500 MHz data show more noise than the 900 MHz data. The reason may be due to overlapping signals caused by reflections from the outer faces of the sand container. This may again be attributed to the larger size of the 500 MHz antenna relative to the dimensions of the sand container. The group velocity within the sand was calculated from the two-way traveltime of events (of reflected and multiple waves) from the metallic plate. In such small-scale experiments the reliability of results can be increased by taking into account the lateral offset and height of antenna-dipoles over the sand surface. A traveltime correction is calculated for the real slightly inclined raypath (rather than for a vertical one) for both antennae (Arcone 1996). The relative dielectric constant ϵ_r is calculated from the velocity using (7); both are plotted as a function of water content G in Figs 9a and b.

The measurements show a decrease in velocity v and an increase in the dielectric constant ϵ_r with increasing water content. In general the results show a good quantitative correlation with the empirical relationships obtained by many authors (e.g. Topp *et al.* 1980; Greaves *et al.* 1996). The small deviation of our data ($\pm 3\%$) can be related to different sample sizes, the degree of grain sorting, clay content and the techniques used in these studies. For example Heßland and Schikowsky (1997) used the TDR technique and HP-analyser.

It is clear that velocity values for the 900 MHz antenna are systematically higher than those for the 500 MHz antenna. However, this velocity difference is relatively small and may be attributed to measurement errors as described above. In this respect, previous experimental data show an inverse relationship between $\sqrt{\epsilon_r}$ and the frequency f in

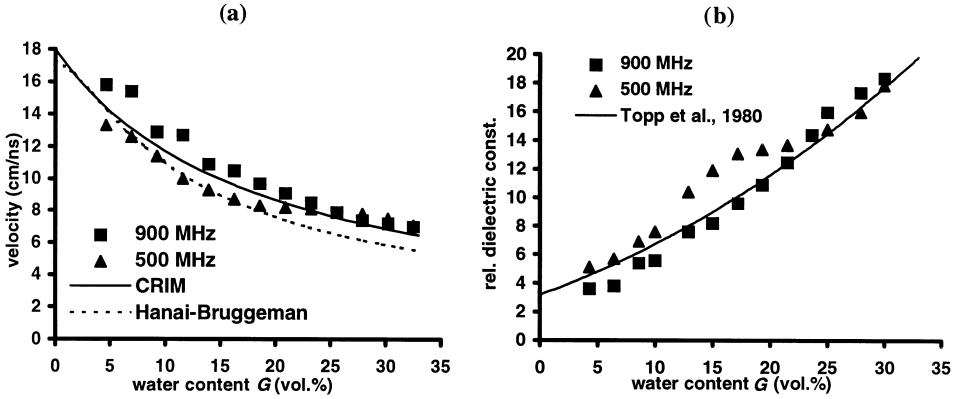

Figure 9. Laboratory measurements using 500 MHz and 900 MHz GPR antennae on the sand of Table 2. (a) The GPR velocity versus the water content. Empirical curves from CRIM (equation (14)) and Hanai–Bruggeman (equations (15), (16)) are shown for comparison. (b) The relative dielectric constant (deduced from (14)) versus the water content. The empirical curve of (17) (Topp *et al.* 1980) is shown for comparison. The following values are used in the calculation: dielectric constants of grain and water $(\epsilon_{r,g}, \epsilon_{r,w}) = 4.7$ and 80, respectively; porosity $\phi = 0.33$; GPR wave velocity in water $v_w = 3.4$ cm/ns, and in air $v_{air} = 30$ cm/ns, $v_s = 15.0$ cm/ns (Shen *et al.* 1985; Knight and Nur 1987).

the range 1–3000 MHz (e.g. Wensink 1993). This yields a direct proportionality between v and f (ϵ_r proportional to v). In the intermediate frequency range, the dispersion effect is often neglected. For media with electric conductivity $\sigma < 100$ mS/m, the velocity decreases with f for $f > 900$ MHz (e.g. Davis and Annan 1989). A velocity dependence on frequency as a possible explanation for the difference in v measured by the 900 MHz and 500 MHz antennae should be further investigated for a broader spectral range (such as 200–1500 MHz). Also the CMP technique for velocity determination should be applied to samples with a size much greater than that of the antenna, i.e. to minimize noise content from sample boundaries. Different measurement techniques should be applied to increase the reliability of the results.

Applications for radargram migration

As described above, the full-scale model contains an electrode grid (depth 2 m) and 27 sensors for tensiometer and TDR measurements (three vertical profiles with nine instruments each at a depth interval of 0.2 m, Fig. 2b). Radargrams measured before water infiltration show interference hyperbolae related to the sensors (Fig. 10a). These hyperbolae can mask the useful signals from the infiltrating water front. Furthermore, the radargram clearly shows the model basis at $t = 38$ ns and the electrode grid at $t = 32$ ns. To focus the hyperbolae, the radargram is 2D migrated using Kirchhoff time migration (Yilmaz 1987). For this analysis, the volumetric water content measured by

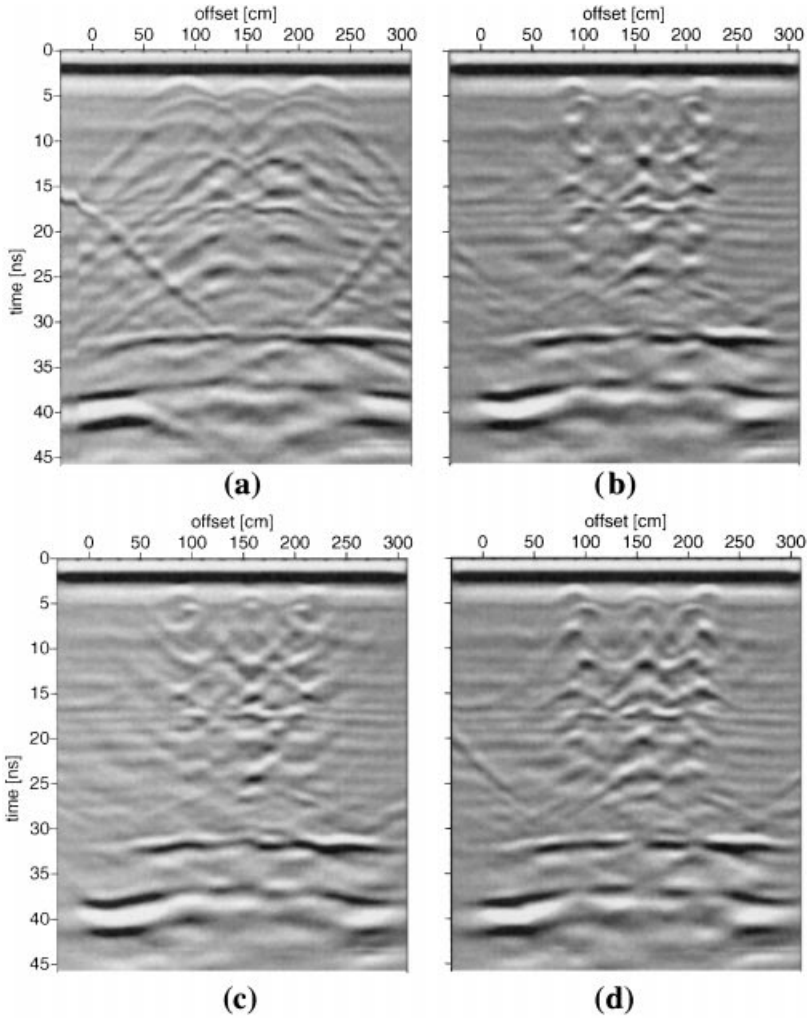

Figure 10. (a) A non-migrated radargram (500 MHz antenna, taken before water infiltration) with strong interfering diffractions from the sensors. (b) A migrated section with the velocities shown in Table 6; note the good separation of diffractions. (c) The same as (a) with 10% increase in velocity; note diffractions with 'smile sign' denoting an undermigration. (d) The same as (a) with 10% decrease in velocity; note the better separation of diffractions indicating that the rms velocity values used for migration (a) are too high.

TDR instruments at the time of survey is replaced in the empirical equation predicted from laboratory data to obtain the relative dielectric constant and average velocity. Using the Dix equation, the interval and rms velocities (v_{int}, v_{rms}) are calculated for a six-layer model (Table 6). The migrated radargrams thus obtained show a clear separation of the individual 27 sensors, even the small horizontally displaced outermost

Table 6. Velocity distribution with depth as deduced from TDR water content at the experimental site of the full-scale model. z: depth; G: water content; ϵ_r: relative dielectric constant; t: traveltime; v, v_{int}, v_{rms}: average, interval and rms velocities, respectively.

z (cm)	G (vol.%)	ϵ_r	v (cm/ns)	t (ns)	v_{int} (cm/ns)	v_{rms} (cm/ns)	z (cm)	G (vol.%)	ϵ_r	v (cm/ns)	t (ns)	v_{int} (cm/ns)	v_{rms} (cm/ns)
20	3.8	3.6	15.8	1.3	16	16.0	140	8.2	4.7	13.8	9.6	14	14.2
40	6.6	4.3	14.5	2.5	15	15.4	160	10.3	5.5	12.8	11.2	13	14.0
60	5.0	3.9	15.2	3.8	15	15.2	180	14.6	7.3	11.1	12.7	11	13.4
80	7.2	4.4	14.3	5.2	14	14.7	200	–	–	–	14.5	10	12.8
100	7.0	4.4	14.3	6.6	14	14.5	220	–	–	–	16.5	10	12.4
120	8.3	4.8	13.7	8.1	14	14.3	240	–	–	–	18.5	10	12.0

instruments along a zigzag line (Fig. 10b). Migration with an increased v_{rms} of 10% shows that diffraction flanks are directed upwards, i.e. the velocity is too high and the radargram is overmigrated as indicated by the upward concave reflections (Fig. 10c). A 10% decrease in v_{rms} results in a clear indication of undermigration (downward convex reflections, Fig. 10d). This result indicates that the migration responds sensitively to small changes in velocity, i.e. the migration can be used for predicting the precise velocity distribution and thus for improving the calibration of TDR for moisture content. An improvement in the results is achieved by using an exact subsurface velocity model which can be obtained by applying the CMP semblance technique.

We conclude that the clear separation of single small targets (diameter 2–3 cm, in a depth range 20–180 cm, at intervals of 20 cm) in the migrated section points towards the high potential of GPR for an exact determination of moisture content and for modelling flow processes in the subsurface in combination with other geophysical and percolation techniques.

Summary and conclusion

This experimental study presents the dependence of propagation parameters of radar waves (reflection coefficient R, velocity v) on pore water salinity and saturation. Controlled experiments were carried out on a homogeneous clean sand in the laboratory and at outdoor sites of predefined model parameters. We arrive at the following conclusions:

1 The reflection coefficient R can be used to distinguish between the three media under investigation which have different pore water salinities: fresh, brackish and saline water. The reflected wave amplitude shows an approximate direct proportionality to the salinity.

2 The salinity evaluation is improved by carrying out a spectral analysis of radar traces; the characterization is more reliable in the frequency domain than in the time domain.

3 A 1D modelling of the reflected wavelet shows a satisfactory agreement in amplitude with the data. The relative reflection amplitude seen in the experimental data may be related on the one hand to the 3D effects of the single bodies at the experimental site and on the other hand to the dependence of the complex relative dielectric contrast on the frequency and conductivity.

4 The GPR technique may be helpful in solving the problem of trade-off between bulk resistivity, water resistivity (salinity) and porosity encountered in applying Archie's equation (Archie 1942) in data interpretation. We suggest that GPR may be useful as a complementary method for salinity evaluation of pore water in the unsaturated vadose zone (contamination studies) and aquifer layer (salinity evaluation).

5 An increase in the water content G causes a decrease in the radar velocity v and an increase in the relative dielectric constant ϵ_r.

6 The G–v and G–ϵ_r relationships deduced for the sand used in this study agree well

with those found by other studies of sediments with different grain size and lithology, as well as with different measurement techniques.

7 The exact focusing of small reflection targets (diameter 2–3 cm, in the depth range 20–180 cm, at intervals of 20 cm) on a migrated radargram shows the high sensitivity of GPR to moisture content and underscores its potential as a complementary technique for the high-resolution mapping of subsurface flow.

8 The reflection amplitudes and velocities for the individual bodies deduced from different techniques show a satisfactory agreement and correlate well with those obtained by other authors.

In an effort to establish empirical relationships between R and pore water salinity, further experiments are being carried out with a finer variation in salinity, different soil materials (grain size) and using antennae of different frequencies. Additional measurements are being taken in the laboratory and field for studying the signal/noise ratio.

The systematic difference, in both G–v and G–ϵ_r curves, between the 500 MHz and 900 MHz antennae should be further studied to clarify whether it is due to external factors, such as 3D effects of the finite laboratory sample relative to that of the antennae, or to dispersion effects.

Acknowledgements

This work was carried out within the framework of project ME 335/96-1, financed by the German Research Foundation (Deutsche Forschungsgemeinschaft, DFG). The authors thank all members of this project, especially Prof. R. Meissner, Prof. W. Rabbel, Dr H. Stümpel, D. Wachsmuth, T. Schubert-Klempnauer, as well as Prof. B. Milkereit and J. Strehlau for critical reading of the manuscript, and the Associate Editor, P. Valla, and the reviewers for their constructive comments and discussions.

References

Archie G.E. 1942. The electrical resistivity log as an aid in determining some reservoir characteristics. *Transactions of the American Institute of Mining Engineers* **146**, 54–62.

Arcone S.A. 1996. High resolution of glacial stratigraphy: a ground-penetrating radar study of Pegasus Runway, McMurdo Station, Antarctica. *Geophysics* **61**, 1653–1663.

Bouwer H. 1978. *Groundwater Hydrology*, p. 360. McGraw-Hill Book Co.

Bugg S.F. and Lloyd J.W. 1976. A study of fresh water lens configuration in the Cayman Islands using resistivity methods. *Quaternary Journal of Engineering Geology* **9**, 291–302.

Buttkus B. 1991. *Spektralanalyse und Filtertheorie in der Angewandten Geophysik*, p. 76. Springer-Verlag, Inc.

Cant R.V. and Weech P.S. 1986. A review of the factors affecting the development of Ghyben-Herzberg lenses in the Bahamas. *Journal of Hydrology* **84**, 333–343.

Davis J.L. and Annan A.P. 1989. Ground-penetrating radar for high-resolution mapping of soil and rock stratigraphy. *Geophysical Prospecting* **37**, 531–551.

Endres A.L. and Knight R. 1992. A theoretical treatment of the effect of microscopic fluid

distribution on the dielectric properties of partially saturated rocks. *Geophysical Prospecting* **40,** 307–324.

Fretwell J.D. and Stewart M.T. 1981. Resistivity study of a coastal Karst terrain, Florida. *Ground Water* **19,** 156–162.

Ghyben B.W. 1888. Nota in verband met de voorgenomen putboring nabij Amsterdam. *Tijdschrift van het Koninklijk Instituut van Ingenieurs*, 21 pp.

Göttsche F.M. 1997. *Identification of cavities by extraction of characteristic parameters from ground probing radar reflection data*. PhD thesis, Christian-Albrechts-Universität zu Kiel.

Greaves R.J., Lesmes D.P., Lee J.M. and Toksöz M.N. 1996. Velocity variations and water content estimated from multi-offset, ground-penetrating radar. *Geophysics* **61,** 683–695.

Guéguen Y. and Palciausskas V. 1994. *Introduction to the Physics of Rocks*. Princeton University Press.

Hagrey S.A. and Michaelsen J. 1996. Tracing soil water flow using resistivity and percolation methods at Bokhorst, Germany. 2nd EEGS meeting, Nantes, France, Expanded Abstracts, 322–325.

Hagrey S.A. and Michaelsen J. 1999. Resistivity and percolation study of preferential flow in vadose zone at Bokhorst, Germany. *Geophysics* **64,** 746–753.

Hagrey S.A., Schubert-Klempnauer T., Wachsmuth D., Michaelsen J. and Meissner R. 1998. Flow paths in a full-scale model. 4th EEGS meeting, Barcelona, Spain, Expanded Abstracts, 271–274.

Hagrey S.A., Schubert-Klempnauer T., Wachsmuth D., Michaelsen J. and Meissner R. 1999. Preferential flow: first results of a full-scale flow model. *Geophysical Journal International* **138,** 643–654.

Hayt W. 1989. *Engineering Electromagnetics*. McGraw-Hill Book Co.

Herzberg B. 1901. Die Wasserversorgung einiger Nordseebäder. *Münichen J. Gasbeleucht. Verwandte Beleuchtungsarten Wasserversorgung* **44,** 815–844.

Heßland T. and Schikowsky P. 1997. Influence of fluids in sediments on the velocity of electromagnetic waves. II GPR-Workshop, Karlsruhe, Germany, Expanded Abstracts, 6–7.

Jackson P.D., Taylor Smith D. and Stanford P.N. 1978. Resistivity-porosity-particle shape relationships for marine sands. *Geophysics* **43,** 1250–1268.

Keller G.V. and Frischknecht F.C. 1966. *Electrical Methods in Geophysical Prospecting*. Pergamon Press, Inc.

Knight R.J. and Nur A. 1987. The dielectric constant of sandstones 60 kHz to 4 MHz. *Geophysics* **52,** 644–654.

Lorrain P., Corson D.R. and Lorrain F. 1995. *Elektromagnetische Felder und Wellen*. W. de Gruyter.

Olhoeft G.R. 1987. Electrical properties from 10^{-3} Hz to 10^{9} Hz – physics and chemistry. *AIP Conference Proceedings* **154,** 281–298.

Schachtschabel P., Blume H.-P., Brümmer G., Hartge K.-H. and Schwertmann U. 1992. *Lehrbuch der Bodenkunde*, pp. 21–25. Ferdinand Enke-Verlag.

Schön J. 1983. *Petrophysik*, pp. 214–286. Ferdinand Enke-Verlag.

Sen P.N. 1981. Relation of certain geometrical features to the dielectric anomaly of rocks. *Geophysics* **46,** 1714–1720.

Sen P.N., Scala C. and Cohen M.H. 1981. A self-similar model for sedimentary rocks with application to the dielectric constant of fused glass beads. *Geophysics* **46,** 781–795.

Shen L.C., Savre W.C., Price J.M. and Athavale K. 1985. Dielectric properties of reservoir rocks at ultra-high frequencies. *Geophysics* **50,** 692–704.

Stolte C. 1994. *E-migration image enhancement for subsurface objects of constant curvature in ground probing radar reflection data*. PhD thesis, Christian-Albrechts-Universität zu Kiel.

Topp G.C., Davis J.L. and Annan A.P. 1980. Electromagnetic determination of soil water content. Measurements in coaxial transmission lines. *Water Resources Research* **16,** 574–582.

Ward S.H. and Hohmann G.H. 1988. Electromagnetic theory for geophysical applications. In: *Electro-magnetic Methods in Applied Geophysics, Vol. 1, Theory* (ed. M.N. Nabighian), pp. 130–311. SEG, Tulsa, OK.

Wensink W.A. 1993. Dielectric properties of wet soils in the frequency range 1–3000 MHz. *Geophysical Prospecting* **41,** 671–696.

Worthington P.F. 1976. Hydrogeophysical equivalence of water salinity, porosity, and matrix conduction in arenaceous aquifers. *Ground Water* **14,** 224–232.

Wyllie M.R.J. and Gregory A.R. 1953. Formation factors of unconsolidated porous media: influence of particle shape and effect of cementation. *Petroleum Transactions AIME* **198,** 103–110.

Yilmaz O. 1987. *Seismic Data Processing*, pp. 240–353. SEG, Tulsa, OK.